Phase-field crystal for an antiferromagnet with elastic interactions

Niloufar Faghihi,[1] Simiso Mkhonta,[2] Ken Elder,[3] and Martin Grant[1]
[1]*Physics Department, Rutherford Building, 3600 rue University, McGill University, Montréal, Québec, Canada H3A 2T8*
[2]*Department of Physics, University of Swaziland, Private Bag 4, Kwaluseni M201, Swaziland*
[3]*Department of Physics, Oakland University, Rochester, Michigan 48309, USA*

(Received 8 February 2019; published 21 August 2019)

We introduce a model which contains the essential elements to formulate and study antiferromagnetism, using the phase-field crystal framework. We focus on the question of how magneto-elastic coupling could lift the frustration in the two-dimensional hexagonal antiferromagnetic phase. Using simulations we observe a rich variety of different phases stable in this model. To characterize different phases we calculate the chiral order parameter and identify the scaling behavior of this order parameter. Furthermore, we observe that vortices appear and are stable close to the nonmagnetic defects. Finally, we studied the ferrimagnetic and spin-flop phase transition in the presence of an external magnetic field.

DOI: 10.1103/PhysRevE.100.022128

I. INTRODUCTION

In a geometrically frustrated magnet the symmetry of the lattice inhibits every pairwise interaction of the system to be satisfied concurrently. For example, antiferromagnetic spins on a two-dimensional triangular lattice have three neighboring spins which can not be pairwise antialigned, and so the system is frustrated. Such two-dimensional frustrated antiferromagnetic systems have been the subject of several theoretical [1–9] as well as experimental studies [10–13]. Geometrical frustration often gives rise to a series of degenerate ground states rather than a single stable ground state [14]. As a result even a minimal perturbation to the Hamiltonian can induce significant changes, selecting one specific ground state.

One of the perturbations that can lift the ground state degeneracy of a frustrated Ising (or Heisenberg) lattice is magnetoelastic coupling and has been the subject of many experimental studies [15–18]. A coupling between the elastic and magnetic degrees of freedom removes the ground state degeneracy by distorting the lattice [19]. Chen and Kardar calculated the phase diagram of an elastic antiferromagnetic system on a triangular lattice [19]. Depending on the system parameters the following phases are stable: disordered, stripe, helical, and ferromagnetic. In the stripe phase, the original triangular structure is deformed, one set of bonds are expanded, and the other two sets are contracted so that the degeneracy of the ground state is removed.

In this paper we apply the phase-field crystal (PFC) approach to study how magnetoelastic coupling can give rise to the removal of magnetic frustration. Moreover we report magnetic frustration causes phase transformation in antiferromagnetic materials.

The PFC approach is a powerful computational method to study microstructure formation in diffusive (mesoscopic) timescales and the atomic length scales [20–22]. It has been applied to study different phenomena such as nucleation, polycrystalline solidification, grain boundaries, and dislocations [23–28]. The main idea of the PFC approach is that the free energy is minimized by structures that are periodic in space with the symmetries of the crystal phases such as hexagonal in two dimensions and body centered cubic (BCC) in three dimensions. It was shown that the free energy of the PFC can be crudely derived from the the classical density functional theory of freezing, by retaining only the first peak in the two-point correlation function [29]. This minimal model can capture the basic elastic and plastic effects [21] but benefits from representing atoms as low-amplitude periodic modulation that are computationally simpler to simulate.

The PFC formalism has been exploited to study multiferroic materials. To study the interrelation between magnetic and elastic properties of ferromagnetic solid, the original PFC kernel was coupled to the Ginzburg-Landau free energy for a ferromagnetic phase transition [30]. The position of the Curie line in the phase diagram as a function of the temperature and the mean density of the system was calculated. Using an amplitude expansion method and elastic calculations the relationship between elastic strains and magnetization was calculated. It was shown that the existence of a grain boundary facilitates the formation of the magnetic domains. Also the influence of the grain misorientation on the magnetic coercivity of the system was studied. In another study [31] the free energy of the structural PFC model [32–34] was coupled to the order parameters describing ferromagnetic and ferroelectric ordering, as well as to the solute impurity field. In this study the position of Curie line was calculated on the liquid-BCC-FCC (face centered cubic) phase transition region on the phase diagram. Using the elastic calculations this model also extended the original magneto-PFC introduced in Ref. [30] to include the (magnetic and electric) anisotropy, and the effect of an external magnetic field on the grain orientation was investigated. Furthermore the relationship between the electric coercivity and grain size was considered.

The formation of magnetic islands and the influence of an external magnetic field on phase transformation has been investigated in Ref. [35]. In this study the multimode PFC

free energy [36] was coupled to the magnetic order parameter. Unlike the two previous studies on magnetoelastic PFC models in which the magnetization modulations were much larger than the the atomic length scales, in this case a coupling term was introduced so that the magnetic moments are localized on the atomic sites and the magnetization is zero in the distances between the density peaks.

In this paper, we couple the original PFC free energy to magnetism to provide an alternative approach to study antiferromagnetism. Using a pseudospectral algorithm in the message passing interface (MPI) framework we conducted simulations in two dimensions. We observe that a triangular phase is not stable in the presence of the antiferromagnetic interaction, and the system goes through a phase transition from a triangular phase to a square phase. We also studied the stability diagram of the system and confirmed that the stripe, helical, square, and ferromagnetic phases can be stabilized depending on two parameters of the free energy: one of the parameters characterizes the stiffness of the crystalline structure of the phase-field crystal formalism, and the other parameter is related to how strong the magnetic and elastic degrees of freedom are coupled to each other.

Furthermore, we studied the growth of a helical phase in a square lattice, and we have evidence to support the idea that this dynamics is overdamped. As well, vortices form close to the grain boundaries. This is in agreement with experimental and theoretical studies that suggest that nonmagnetic impurities stabilize vortices [37,38]. Finally, we studied the behavior of the system in the presence of an external magnetic field and observed a stable ferrimagnetic phase as well as what we believe is a novel spin-flop phase, arising from an initially helical state.

II. FREE ENERGY FUNCTIONAL

We propose the model for an antiferromagnet by modifying the Landau-Ginzburg ferromagnetic free energy [39] as

$$F_{AF}=\int d\vec{r}\left\{-W_0^2|\nabla\vec{m}|^2+|\nabla^2\vec{m}|^2+\frac{r_N}{2}|\vec{m}|^2+\frac{\gamma}{4}|\vec{m}|^4-\vec{m}\cdot\vec{B}\right\}. \tag{1}$$

The term $-W_0^2|\nabla\vec{m}|^2$, unlike the normal Landau-Ginzburg free energy for a ferromagnetic phase transition, has a negative sign which makes it favorable for the neighboring spins to have spatial gradients. But in order for the free energy to have finite gradients we need to add the next order in terms of the gradients, consistent with the symmetries of the system. In this case this term is the fourth-order gradient term. Similar to the arguments of the phase-field-crystal model [20,21] this free energy favors a length scale which corresponds to the equilibrium periodicity of the system. In this free energy, W_0, r_N, and γ are phenomenological constants. W_0 sets the length scale for the antiferromagnetic order, r_N is related to the Néel's temperature of antiferromagnetic phase transition, and γ is related to the saturation magnetization and magnetic susceptibility of the system. The term $\vec{m}\cdot\vec{B}$ accounts for the interaction between the external magnetic field, $\vec{B}$, and the magnetization vectors, $\vec{m}$.

We couple this magnetic interaction with the classical phase-field-crystal formalism (PFC) [20,21] for crystal growth,

$$F_{\mathrm{PFC}}=\beta\int d\vec{r}\left\{\frac{\psi}{2}\left(q_0^2+\nabla^2\right)^2\psi+\frac{r}{2}\psi^2+\frac{\psi^4}{4}\right\}, \tag{2}$$

where ψ is the particle number density and r and q_0 are phenomenological constants. The phase diagram of this model consists of a liquid phase, a stripe phase, and a hexagonal phase. The wave vector magnitude q_0 determines the lattice constant of the equilibrium phase. The bulk free energy terms produce the two-well curve as a function of the order parameter, which favors one of the two phases of liquid or solid depending on the temperature, r, and the mean density of the system. The parameter β acts as the crystal stiffness coefficient. The larger the value of β, the stiffer the PFC crystal.

We propose the coupling free energy to have the simple form

$$F_C=\int d\vec{r}\{-\alpha\vec{m}^2\psi\}, \tag{3}$$

where α is a parameter which determines the strength of the coupling between the density and magnetization fields. This equation guarantees that the magnetic moments are localized on the atomic sites and the magnetic islands form [35].

In order to conduct simulations we solve dissipative dynamics to minimize the free energy. We use conserved dynamics (model B) for the density field (ψ) and nonconserved dynamics (model A) for the magnetization fields [$\vec{m}=(m_x,m_y)$]:

$$\frac{\partial\psi}{\partial t}=\mu_\psi\nabla^2\left(\frac{\delta F}{\delta\psi}\right) \tag{4}$$

for the density and

$$\frac{\partial m_i}{\partial t}=-\mu_m\frac{\delta F}{\delta m_i} \tag{5}$$

for the magnetization, where $F=F_{AF}+F_{\mathrm{PFC}}+F_C$ is the total free energy of the system and m_i refers to m_x or m_y. In these equations, μ_ψ is the mobility of the density field and μ_m is the mobility of the magnetization field, and in general they can be different.

In the following simulations we implemented periodic boundary conditions, and unless otherwise stated, the parameters of the free energy are chosen as $(q_0, r, W_0, r_N, \gamma)=(1, -0.15, 1, -0.1, 1)$ and $\vec{B}=0$.

III. RESULTS

A. Stability diagram

We checked the stability of the helical, stripe, square, ferromagnetic, and disordered phase, and we find the regions in the α-β phase diagram in which various phases are stable. One point to note is that in order to depict the magnetization field more clearly, we developed a method which identifies the magnetic islands separately. Each magnetic island corresponds to an atomic site. We then calculate the mean value of the magnetization vectors at each island and depict the average value as a single arrow on the center of each island, as shown in Fig. 1. Therefore each arrow in the inset of Fig. 1 depicts the average magnetization at each atomic site.

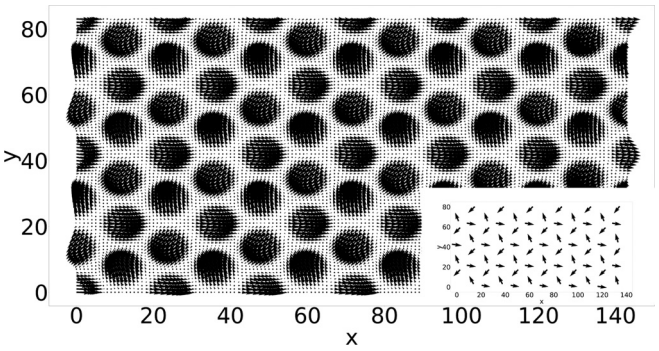

FIG. 1. Configuration of the magnetization field. It should be mentioned that the small magnetic moments existing between the atoms are on average of order of 0.25 or less, while the moments on atomistic sites are on average of order of 1.75 or more. Inset: Arrows depict the magnetization field averaged over each atomic site. The system size is $144dx \times 84dy$, and each island's radius is roughly $7dx$, where dx and dy are the simulation's mesh sizes in the x and y directions, respectively.

We run the single-mode PFC model as defined in Eq. (2), yet we find a square phase is stable in certain regions of the phase diagram. This is interesting because the phase diagram of the single-mode PFC model does not predict a square phase. The reason we can stabilize the square phase with the single-mode PFC, as we will see in more detail, is the coupling to the antiferromagnetic free energy in Eq. (1). The configurations of the perfect helical, stripe, and square phases are presented in Fig. 2. Moreover, the disordered phase is obtained when $r_N > 0$ in Eq. (1).

We ran two series of simulations, and in both we used the following values for the temperature and mean density: $(r, \psi_0) = (-0.15, 0.2)$. In the first series we started from the perfect stripe, perfect helical, perfect square, and perfect hexagonal ferromagnetic phases, separately, and calculated the energy of the system by letting the system equilibrate. We prepared the perfect helical phase by starting from a system with the minimum number of particles needed to model a helical phase, i.e., six particles. For the helical and stripe phases which have hexagonal symmetries we chose $dy = [L_x dx/(\sqrt{3}L_y)]$ so that a particle can perfectly fit inside the simulation box in a hexagonal lattice, where L_x and L_y are the system dimensions and dx and dy are the simulation's mesh sizes.

In order to find the lattice constant value, $a_x = L_x dx$, that minimizes the free energy, we manually varied a_x and calculated the free energy. We repeated this process to find the a_x for which the free energy is minimized. The values of mean energy as a function of a_x are shown in the inset of Fig. 3(a) for a stripe phase with $\alpha = 1$ and $\beta = 3$.

For each value of α and β we performed the procedure explained above and found the correct value of a_x. We then run the simulation to equilibrate the system using the correct value of a_x and calculated the free energy as a function of β for each value of $\alpha = 0.5, 1, 1.5$.

We also prepared a perfect ferromagnetic phase and a perfect square phase to compare their free energies to the free energies of the helical and stripe phases. The plots of the free

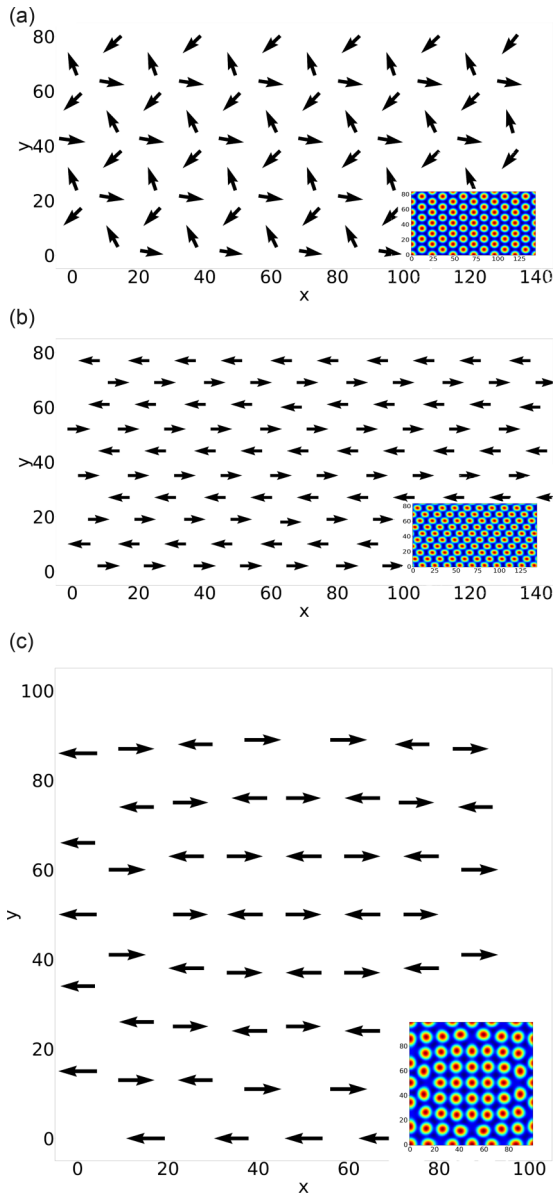

FIG. 2. (a) Configuration of the magnetization vectors of a perfect helical phase; inset (a): the density field corresponding to the helical phase. (b) Configuration of the magnetization vectors of a perfect stripe phase; inset (b): the density field corresponding to the stripe phase. The density field of a stripe phase contains a deformed hexagonal structure, in such a way that the magnetic frustration is lifted. (c) Antiferromagnetic square phase; inset (c): the corresponding density. In order to produce a perfect square phase, the shape of the simulation box should be of the form of a square as well. That is why the scale of panel (c) is different from panels (a) and (b).

energy as a function of β are shown in Figs. 3(a) and 3(b) for $\alpha = 0.5, 1, 1.5$, respectively.

From these figures we can determine which phase is more stable for each value of α and β. For $\alpha = 0.5$, Fig. 3(a) shows that the helical phase is more stable than the stripe phase. In this diagram the energies of the square phase are not plotted because we could not find a stable square phase in this range of parameters except at $\beta = 1$ for which the energy is about the same value of the energy of the helical phase. In this case,

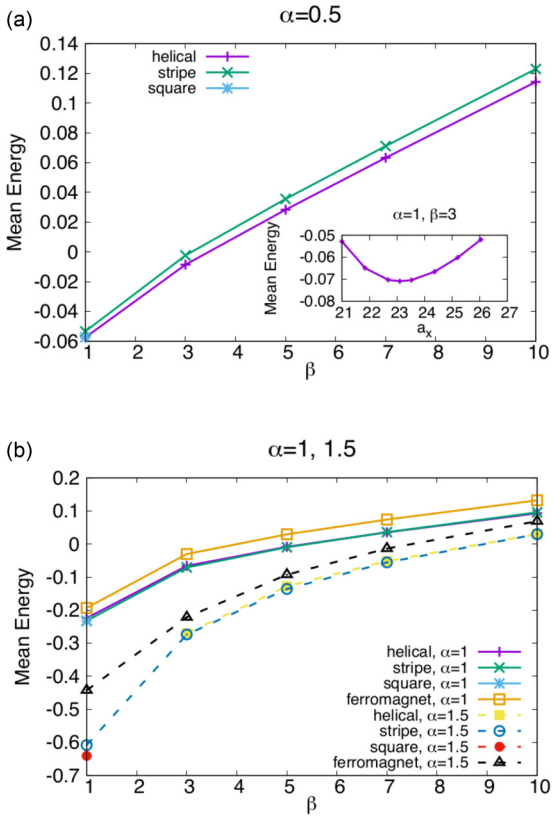

FIG. 3. (a) Free energies of the perfect stripe, helical, and square phases as a function of β for $\alpha = 0.5$. There is not any ferromagnetic free energy in this plot because we could not stabilize any ferromagnetic phase with these parameters. The simulations are done at $\beta = 1, 3, 5, 7, 10$, and the lines are plotted to guide the eye. Inset: The plot of the mean energy of the system as a function of the lattice constant, a_x, for a stripe phase with $\alpha = 1$ and $\beta = 3$. In this case, the minimum mean energy of -0.071 occurs at $a_x = 23.1$ (b) Free energies of the perfect stripe, helical, and square and ferromagnetic phases as a function of β for $\alpha = 1$ and $\alpha = 1.5$.

we determined whether a helical phase or the square phase is the more stable phase by looking at the configurations from simulations that will follow.

For $\alpha = 1$ Fig. 3(b) shows that the ferromagnetic phase has a larger free energy and hence cannot be the stable phase. This figure also shows that for $\beta \leqslant 7$ the stripe phase is more stable, but for $\beta > 7$ the helical phase becomes more stable. Finally for $\alpha = 1.5$ the square phase is more stable for $\beta = 1$. For the rest of the β values the stripe phase is more stable.

Since the free energies of the helical and stripe phases are very close, we designed a simulation to better identify the more stable phase. In the second series of simulations we prepare the system in an initial condition in which the stripe and helical phases coexist. A slab of the helical phase was placed in a box filled with the stripe phase. The total system size was 84×144. This simulation was conducted to check the competition between the stripe and helical phases and which phase is more stable at each α and β value. We noticed that for each constant value of α, as β is increased, the stability of the helical phase increases. Also for a constant value of β, as α is increased, the stripe phase becomes more stable. For very small values of β and for larger values of α the square phase becomes more stable. The stripe and helical configurations shown in Figs. 4(a) and 4(b) are two configurations of the system at $\alpha = 1$, $\beta = 10$ and $\alpha = 1.5$, $\beta = 3$, respectively.

The results of these simulations are summarized in the stability diagram of Fig. 5. The continuous lines are plotted by interpolating the simulation results performed at different regions of the diagram. We expect coexistence regions for square-stripe and stripe-helical phases, and each of the phases will stabilize at different densities which would give coexistence points, but these points would lie along a third (density) axis and we did not calculate those regions.

It should be mentioned that for $\alpha = 1$ and $\alpha = 1.5$ with $\beta = 1$, these simulations converge to the square phase, for which the density field is shown in Fig. 4(c). This is interesting as the phase-field crystal model we are implementing is the one-mode PFC formalism in which based on Ref. [21] no square phase is stable in this model. However, the antiferromagnetic interaction dictates a phase transformation from hexagonal to square phase. The reason is that the antiferromagnetic interaction on a hexagonal lattice cannot be satisfied while it can perfectly take advantage of coupling to a square lattice. The square phase, however, is not stable at large values of β. The reason is that large β means there is a strong phase-field crystal elastic energy which favors the hexagonal phase.

These results are consistent with those obtained from the energy calculations. For $\alpha = 1$ and small value of $\beta = 1$ the square phase is more stable. The system never converges to a ferromagnetic phase, which is in agreement with the energy calculations where the energy of the ferromagnetic phase is larger than all the other three phases for all of the β values.

B. Chirality

To obtain a better understanding of the phase diagram, we characterize the helical phase using the chiral order parameter defined as [40,41]

$$\kappa_p = \frac{2}{3\sqrt{3}} \sum_{\langle ij \rangle \in p} \left(S_i^x S_j^y - S_i^y S_j^x \right), \tag{6}$$

where S_i and S_j are the normalized magnetization vectors on each lattice point and the summation, $\sum_{\langle ij \rangle \in p}$, runs over the three directed bonds surrounding each plaquette, p. Physically, the chirality captures the sense of the noncollinear 120° structure.

The chirality values are consistent with the stability diagram's results. We run simulations similar to those in Sec. III A except that instead of starting from a coexistence of stripe and helical, we start them from the configuration of the perfect helical phase and let the system equilibrate. For $\beta = 3$ and $\alpha = 1.5$, the chirality is obtained to be, to two significant figures, $\kappa_p = 0.00028$, where, as expected for a stripe phase, the chirality is very small (theoretically zero). If $\beta = 1$ and $\alpha = 0.5$, we have the helical phase with $\kappa_p = 0.87$. As we increase β the hexagonal phase become stiffer and more stable and the square phase less stable. For $\beta = 9$ and $\alpha = 1$ the chirality is $\kappa_p \approx 1$.

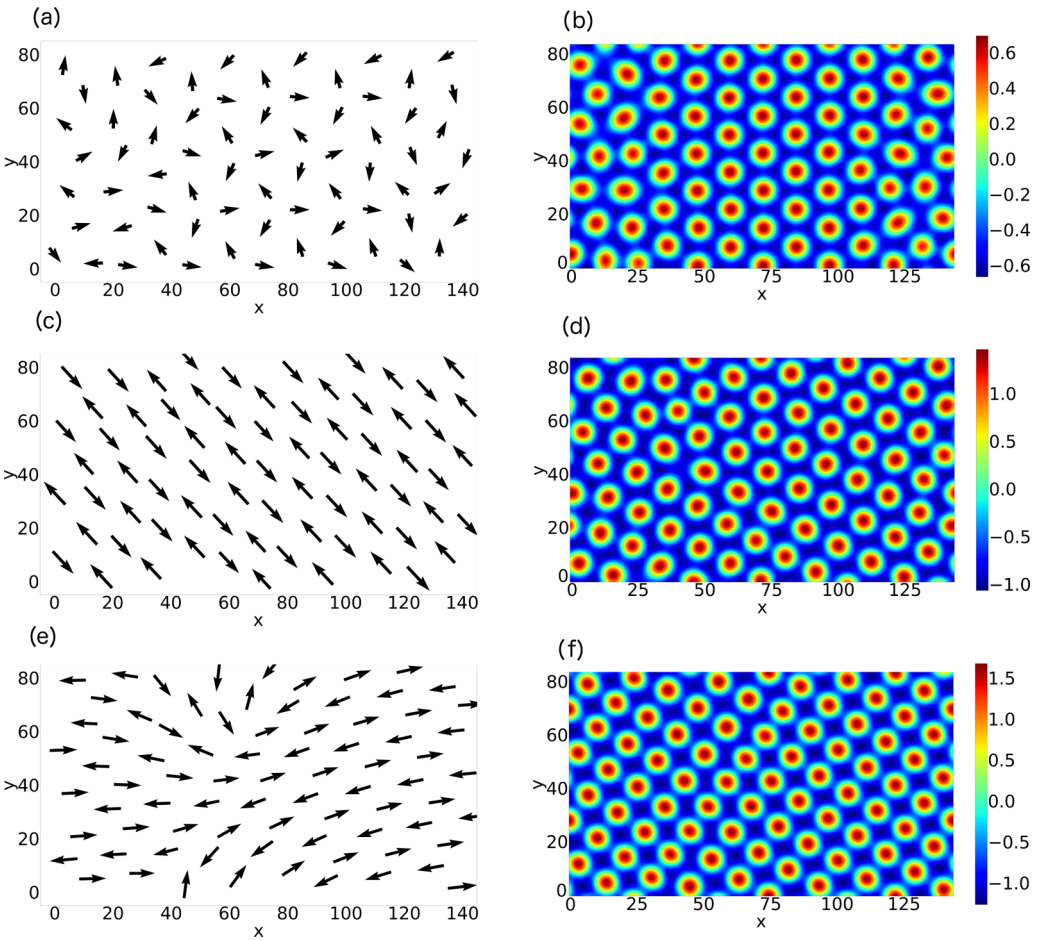

FIG. 4. (a) The magnetization vectors on a helical phase obtained at $\alpha = 1$ and $\beta = 10$. (b) The corresponding density field, showing hexagonal symmetry. (c) The magnetization vectors in a hexagonal stripe phase at $\alpha = 1.5$ and $\beta = 3$. (d) The corresponding density field, showing a stripe (deformed hexagonal symmetry) phase. (e) The magnetization configuration of the square phase obtained from antiferromagnetic one-mode phase-field-crystal formalism with $\alpha = 1$ and $\beta = 1$. (f) The corresponding density field, showing square symmetry.

C. Chirality as a function of time

Starting the simulation from two square structures with a symmetric grain boundary in the middle of the simulation box, we prepared the system parameters corresponding to a helical equilibrium phase, i.e., $(\alpha, \beta) = (0.5, 1)$. We chose the mesh size to be $dx = dy = 0.5$ and the size of the system is 1024×1024. The time step is $dt = 0.01$ for the evolution of the density field and $dt_m = 0.1$ for the evolution of the magnetization field. This means that we set $\mu_m/\mu_\psi = 10$ in Eqs. (4) and (5). We chose $dt_m > dt$ because we intended to allow for the magnetization vectors to form a chiral configuration in the regions already phase transformed to hexagonal. As we ran the simulation, we noticed that the hexagonal phase started to form from the grain boundary. Figures 6(a) and 6(b) show the configuration of the density field for the early time in simulations and final step of the simulation, respectively. We used different colors to show the atomic positions with number of neighbors not equal to four (blue) as opposed to the atomic positions with number of neighbors equal to four, i.e., a square lattice (red). It can be seen in Fig. 6(a) that the helical phase starts to grow from the grain boundaries. Furthermore, in the later times it can be seen that the chiral phase is nucleated from the defect regions.

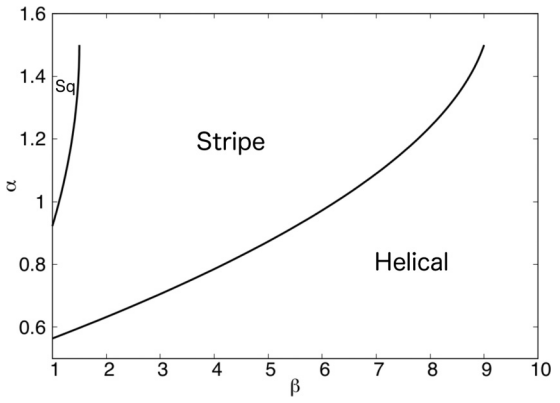

FIG. 5. Stability diagram of the system obtained from full system simulations. Three phases are stable for different values of α and β: square, stripe, and helical.

Calculating the chirality, we observe that this hexagonal phase is a helical antiferromagnetic phase, as expected. We calculated the chirality as a function of time and noted that it increases with time, as the helical phase grows.

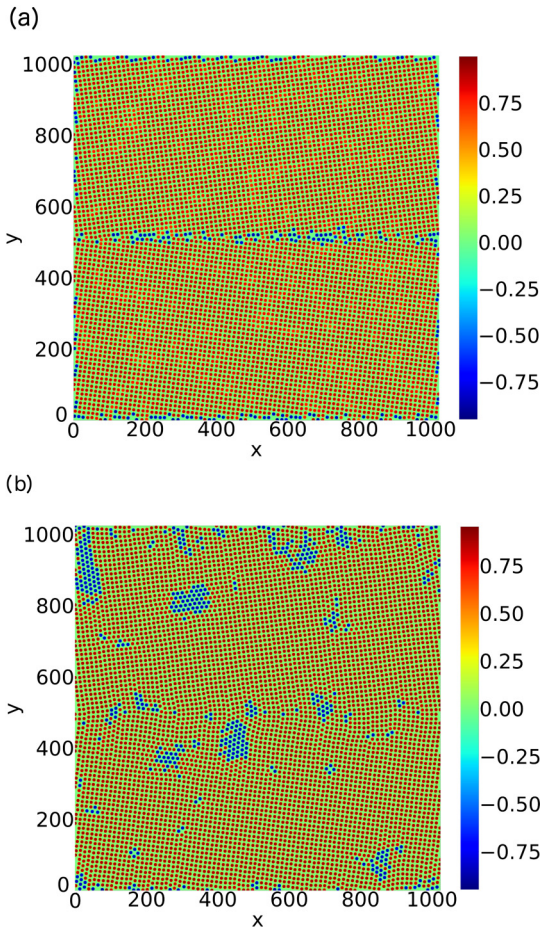

FIG. 6. (a) Density field of the helical phase (blue) starting to grow from the grain boundary in the square lattice (red), at the early time step of $t = 2 \times 10^3 dt$. (b) Density field of the helical phase (blue) grown in the square lattice (red), at the late time step of $t = 10^5 dt$.

It should be mentioned that in the process of calculation of the chirality, we first find the plaquettes and then calculate Eq. (6). As a result when calculating the total chirality over the whole system, the square phase does not have any contribution [42].

Analyzing the scaling behavior of the chirality as a function of time, we can fit the chirality versus time curve to an exponential function. We expect such behavior as this is an overdamped system attempting to minimize the free energy. Therefore, we can write the differential equation governing the chirality as $d^2\kappa/dt^2 = (-1/\tau)d\kappa/dt$. Solving this equation gives $\kappa(t) = (\kappa_\infty - \kappa_0)(1 - e^{-t/\tau}) + \kappa_0$. Figure 7 shows the chirality as a function of time for the system parameters $(\psi_0, r, W_0, r_N, \alpha, \beta) = (0.25, -0.2, 1, -0.1, 0.5, 1)$ in which we expect a helical configuration for the equilibrium phase. We fit the simulation using the exponential form and obtain the following fitting parameters: $\kappa_0 = 0.63$, $\kappa_\infty = 0.88$, and $\tau = 6400$. If we run the simulations so that the helical phases impinge, we will have domain walls. If the domain walls appear, we expect the dynamics to be slower, i.e., power law scaling.

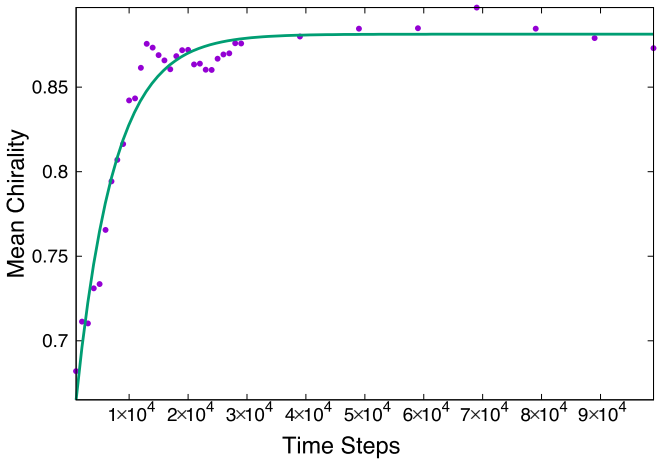

FIG. 7. Purple: chirality as a function of time for a growing helical phase in a square lattice, obtained from simulations. Green: fit to the equation $\kappa(t) = (\kappa_\infty - \kappa_0)(1 - e^{-t/\tau}) + \kappa_0$ with the appropriate parameters. The dynamics of the chirality follows the dynamics of an overdamped system. The values on the time axis are in units of dt_m.

D. Vortices

Vortices have been observed in two-dimensional antiferromagnetic systems [43,44]. It is known that crystalline defects and nonmagnetic impurities tend to stabilize the vortices in antiferromagnetic materials [37,38]. We noticed this happens in our simulations: when the system contains a grain boundary, we observe stabilized vortices. If there is no grain boundary in the system, we do not see any vortices in our simulations. The vortex configuration is shown in Fig. 8. The grain boundary is located along the line of $x = 512$, and there are vortices formed about the grain boundary. We also noticed that in the regions where there is a vortex, there is an increase in the elastic free energy of the system of less than 1%, and in the regions where there is grain boundary, the elastic free energy increases about 1.5%.

E. External magnetic field

To confirm the model can recover well-known phases in antiferromagnetic systems such as the ferrimagnetic and the spin-flop phases, we ran some simulations under the application of an external magnetic field.

1. Ferrimagnetic phase

Starting the simulations from a hexagonal ferromagnetic system with $(r, \psi_0, \alpha, \beta) = (-0.15, 0.2, 1, 1)$, we decreased the value of α from 1, in the presence of an external magnetic field of $\vec{B} = (0.1, 0)$. We noticed that the system undergoes a phase transition to a square ferrimagnetic phase at $\alpha = 0.3$, where the system clearly has a net magnetization. The net magnetization over the unit cell in this case is $m_{\text{net}} = 0.14$. Figure 9 shows the configuration of the ferrimagnetic phase. This phase has been studied previously both theoretically and experimentally [13,45].

2. Spin-flop transition

It is known that by applying an external magnetic field at sufficiently low temperatures, the magnetization vectors

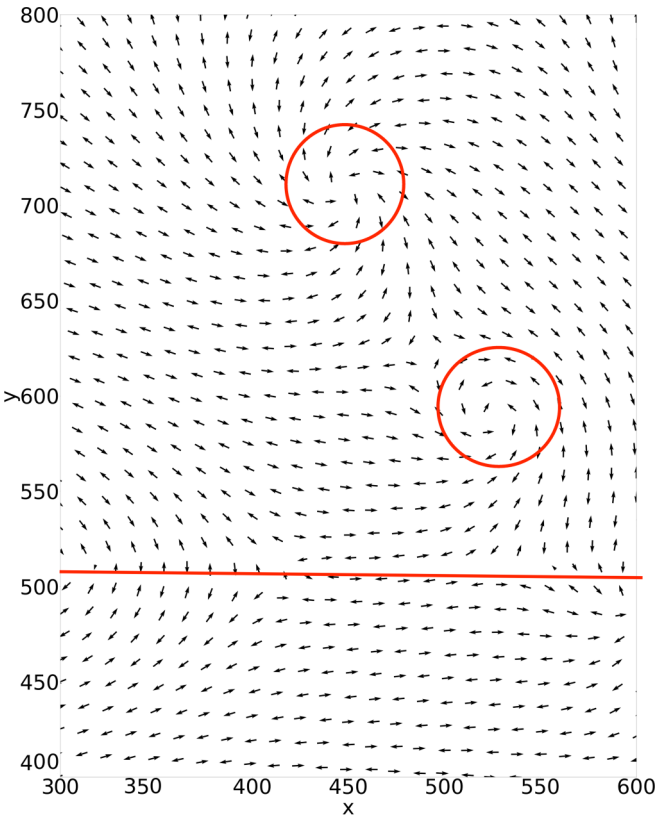

FIG. 8. A snapshot of the magnetization vectors of part of a system of size 1024×1024, close to the grain boundary. The grain boundary is located along the line of $x = 512$ in this configuration. Vortices can be observed, which suggests that grain boundaries and defects stabilize vortices. Two easily seen vortices are encircled. We did not observe any vortices in the absence of a grain boundary.

in an antiferromagnetic material change direction from the easy axis of magnetization to a transverse direction [1,46]. By applying a small external magnetic field to the system at a temperature below the Néel's temperature, if the field is small, the magnetization vectors will be parallel and antiparallel to the easy axis of magnetization. If the field is increased, a phase transition occurs and the magnetization vectors "flop"

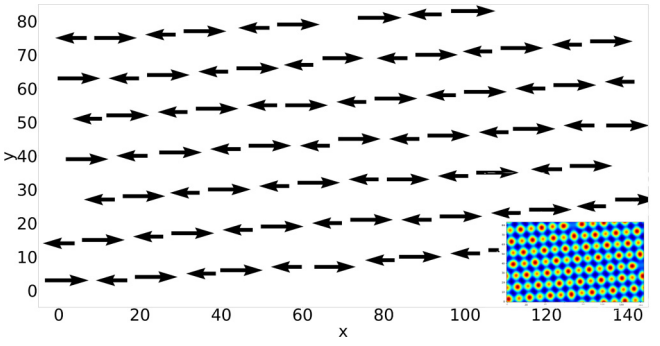

FIG. 9. Configuration of the magnetization vectors of a ferrimagnetic phase in the presence of an external magnetic field $\vec{B} = (0.1, 0)$. Inset: The corresponding density field clearly shows a square symmetry.

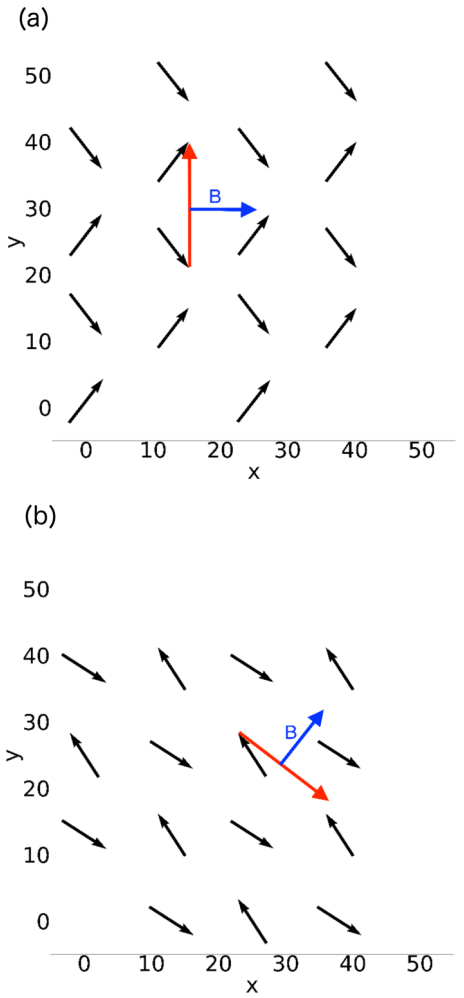

FIG. 10. (a) Spin-flop phase transition when we apply an external field of $\vec{B} = 0.4\hat{x}$. The black arrows depict the magnetization vectors. The subtraction of the two vectors of the sublattice magnetization (the red arrow) lies perpendicular to the applied magnetic field (the blue arrow, labeled "B"). (b) Spin-flop phase transition when we apply an external magnetic field of $\vec{B} = 0.1\hat{x} + 0.1\hat{y}$. The subtraction of the two vectors of the sublattice magnetization lies perpendicular to the applied magnetic field. While the system size is 50×50, we plot these figures for $x \in [-5, 55]$ because we locate the middle of the arrows on each point, and therefore the arrows may start and end out of the size of the system.

to a transverse direction with respect to the external magnetic field. This is the spin-flop phase transition.

In our simulations we observe that by increasing the external magnetic field from zero, the vector $\vec{M}_A - \vec{M}_B$, which is the subtraction of the sublattice magnetizations, will lie perpendicular to the applied magnetic field. In Fig. 10(a) the magnetic field is applied along the x direction on a square lattice: $\vec{B} = 0.4\hat{x}$. We see $\vec{M}_A - \vec{M}_B$ (the red arrow in the figure) lies perpendicular to the magnetic field. If we apply the magnetic field of $\vec{B} = 0.1(\hat{x} + \hat{y})$ we observe that the subtraction vector [the red arrow in Fig. 10(b)] again will be directed perpendicular to the applied magnetic field.

Starting from a helical phase, we applied an external magnetic field in the x direction and increased in steps of

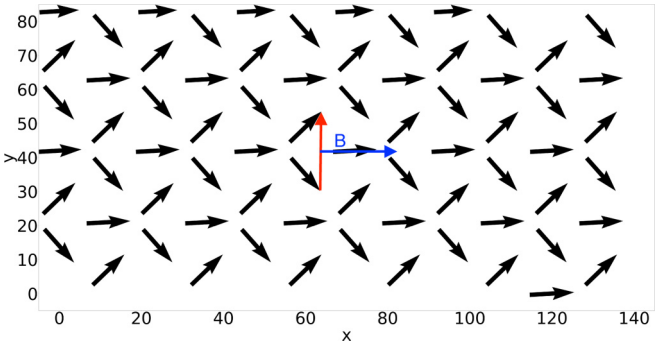

FIG. 11. Spin-flop phase transition when we apply an external magnetic field of $\vec{B} = 0.3\hat{x}$ to an initially helical phase. The black arrows depict the magnetization vectors. The vertical red arrow shows the direction of the subtraction of the square sublattice magnetization, and the horizontal blue arrow (labeled "B") shows the direction of the applied magnetic field.

$\Delta B = 0.05$ until we reach $\vec{B} = 0.3\hat{x}$, where what we believe is a novel spin-flop transition happens (see Fig. 11). It is interesting to see that this spin-flop phase results from an initially chiral state. If we look at the magnetization vectors in the y direction, we see that there are points for which $m_y = 0$. These points lie on a hexagonal lattice with lattice constant two times of the system's hexagonal lattice. In this scheme, as can be seen in Fig. 11, the subtraction of the two sublattice magnetizations on the square lattice (red arrow) lies perpendicular to the applied magnetic field (blue arrow). We observe a similar effect if we apply the external magnetic field in the $\vec{B} = 0.15(\hat{x} + \hat{y})$ direction.

IV. CONCLUSION

We presented a minimal formalism in the framework of the phase-field crystal approach to couple antiferromagnetism and elastic interaction. The model extends the classical Ginzburg-Landau free energy of ferromagnetic phase transitions so that adjacent antiparallel magnetization vectors are favorable. This modified Ginzburg-Landau free energy is coupled to the customary phase-field crystal approach so that the peaks of the magnetization field are located where the atomic sites are located.

We observed that elasticity could lift the magnetic frustration in the two-dimensional hexagonal antiferromagnetic phase. In particular the model stabilizes a square phase in the presence of antiferromagnetic interaction, to avoid the geometrical frustration in the two-dimensional hexagonal antiferromagnetic phase.

Using this model we presented the stability diagram of the system containing square, stripe, helical, and ferromagnetic phases. Conducting simulations we calculated the energy of these competing phases to determine which phase is more stable. Since the energy values of different phases are close, we also performed simulations to check if two phases of stripe and helical phase coexist, which one will take over the simulation box. We also calculated the chirality order parameter for these phases.

Furthermore, we studied the growth of the helical phase in a square phase and calculated the chirality as a function of time. These calculations show that this dynamics is similar to an overdamped dynamics. We confirmed that we could recover the ferrimagnetic phase. Using this model, we also found a spin-flop phase resulting from applying a field to the helical phase.

ACKNOWLEDGMENTS

This work was supported by the NSERC (Natural Sciences and Engineering Research Council of Canada) and by le Fonds de recherche du Québec—Nature et technologies. We acknowledge Compute Canada and SHARCNET for computing resources.

[1] D. P. Landau and K. Binder,Phys. Rev. B **24**, 1391 (1981).
[2] R. Leidl and W. Selke, Phys. Rev. B **70**, 174425 (2004).
[3] D. H. Lee, J. D. Joannopoulos, J. W. Negele, and D. Pl. Landau, Phys. Rev. Lett. **52**, 433 (1984).
[4] D. H. Lee, J. D. Joannopoulos, J. W. Negele, and D. Pl. Landau, Phys. Rev. B **33**, 450 (1986).
[5] D. H. Lee, R. G. Caflisch, J. D. Joannopoulos, and F. Y. Wu, Phys. Rev. B **29**, 2680 (1984).
[6] S. Teitel and C. Jayaprakash, Phys. Rev. B **27**, 598 (1983).
[7] L. Gu, B. Chakraborty, P. L. Garrido, M. Phani, and J. L. Lebowitz, Phys. Rev. B **53**, 11985 (1996).
[8] Y. B. Gaididei, A. Saxena, T. Lookman, A. R. Bishop, and H. Büttner, Phys. Rev. B **66**, 140403(R) (2002).
[9] E. Kim, B. Kim, and S. J. Lee, Phys. Rev. E **68**, 066127 (2003).
[10] T. Ono, H. Tanaka, O. Kolomiyets, H. Mitamura, T. Goto, K. Nakajima, A. Oosawa, Y Koike, K. Kakurai, and J. Klenke, J. Phys.: Condens. Matter **16**, S773 (2004).
[11] R. Coldea, D. A. Tennant, A. M. Tsvelik, and Z. Tylczynski, Phys. Rev. Lett. **86**, 1335 (2001).
[12] R. Coldea, D. A. Tennant, K. Habicht, P. Smeibidl, C. Wolters, and Z. Tylczynski, Phys. Rev. Lett. **88**, 137203 (2002).
[13] I. Krešić, G. Labeyrie, G. R. M. Robb, G.-L. Oppo, P. M. Gomes, P. Griffin, R. Kaiser, and T. Ackemann, Commun. Phys. **1**, 33 (2018).
[14] R. Moessner and P. Ramirez, Phys. Today **59**(2), 24 (2006).
[15] E. Sagi, O. Ofer, A. Keren, and J. S. Gardner, Phys. Rev. Lett. **94**, 237202 (2005).
[16] A. Keren and J. S. Gardner, Phys. Rev. Lett. **87**, 177201 (2001).
[17] J. C. E. Rasch, M. Boehm, C. Ritter, H. Mutka, J. Schefer, L. Keller, G. Abramova, A. Cervellino, and J. F. Löffler, Phys. Rev. B **80**, 104431 (2009).
[18] P. Carretta, N. Papinutto, C. B. Azzoni, M. C. Mozzati, E. Pavarini, S. Gonthier, and P. Millet, Phys. Rev. B **66**, 094420 (2002).
[19] Z.-Y. Chen and M. Kardar, J. Phys. C **19**, 6825 (1986).
[20] K. R. Elder, M. Katakowski, M. Haataja, and M. Grant, Phys. Rev. Lett. **88**, 245701 (2002).
[21] K. R. Elder and M. Grant, Phys. Rev. E **70**, 051605 (2004).

[22] P. F. Tupper and M. Grant, Europhys. Lett. **81**, 40007 (2008).
[23] J. Mellenthin, A. Karma, and M. Plapp, Phys. Rev. B **78**, 184110 (2008).
[24] G. I. Tóth, T. Pusztai, G. Tegze, G. Tóth, and L. Gránásy, Phys. Rev. Lett. **107**, 175702 (2011).
[25] H. Emmerich, H. Löwen, R. Wittkowski, T. Gruhn, G. L. Tóth, G. Tegze, and L. Gránásy, Adv. Phys. **61**, 665 (2012).
[26] L. Gránásy, F. Podmaniczky, G. I. Tóth, G. Tegze, and T. Puszta, Chem. Soc. Rev. **43**, 2159 (2014).
[27] J. Berry, N. Provatas, J. Rottler, and C. W. Sinclair, Phys. Rev. B **86**, 224112 (2012).
[28] J. Berry, N. Provatas, J. Rottler, and C. W. Sinclair, Phys. Rev. B **89**, 214117 (2014).
[29] K. R. Elder, N. Provatas, J. Berry, P. Stefanovic, and M. Grant, Phys. Rev. B **75**, 064107 (2007).
[30] N. Faghihi, N. Provatas, K. R. Elder, M. Grant, and M. Karttunen, Phys. Rev. E **88**, 032407 (2013).
[31] M. Seymour, F. Sanches, K. Elder, and N. Provatas, Phys. Rev. B **92**, 184109 (2015).
[32] M. Greenwood, N. Provatas, and J. Röttler, Phys. Rev. Lett. **105**, 045702 (2010).
[33] M. Greenwood, J. Röttler, and N. Provatas, Phys. Rev. E **83**, 031601 (2011).
[34] M. Greenwood, N. Ofori-Opoku, J. Röttler, and N. Provatas, Phys. Rev. B **84**, 064104 (2011).
[35] N. Faghihi, S. Mkhonta, K. R. Elder, and M. Grant, Eur. Phys. J. B **91**, 55 (2018).
[36] S. K. Mkhonta, K. R. Elder, and Z.-F. Huang, Phys. Rev. Lett. **111**, 035501 (2013).
[37] A. R. Pereira and G. M. Wysin, Phys. Rev. B **73**, 214402 (2006).
[38] K. Subbaraman, C. E. Zaspel, and J. E. Drumheller, Phys. Rev. Lett. **80**, 2201 (1998).
[39] P. M. Chaikin and T. C Lubensky, *Principles of Condensed Matter Physics* (Cambridge University Press, Cambridge, 2000).
[40] H. Kawamura, J. Appl. Phys. **63**, 3086 (1988).
[41] T. Obuchi and H. Kawamura, J. Phys. Soc. Jpn. **81**, 054003 (2012).
[42] To calculate the chirality we need to find the nearest neighbors of the ith atomic site, therefore we need a threshold distance, d_0, based on which we can decide whether an arbitrary atom is a neighbor to the ith atom or not. We chose d_0 by knowing the value of the interatomic distance in a hexagonal lattice in the phase-field crystal formalism (with the chosen free energy parameters) and adopting a value for d_0 which is slightly larger than the interatomic distance.
[43] F. P. Chmiel, N. W. Price, R. D. Johnson, A. D. Lamirand, J. Schad, G. van der Laan, D. T. Harris, J. Irwin, M. S. Rzchowski, C. B. Eom *et al.*, Nat. Mater. **17**, 581 (2018).
[44] J. Wu, D. Carlton, J. S. Park, Y. Meng, E. Arenholz, A. Doran, A. T. Young, A. Scholl, C. Hwang, H. W. Zhao *et al.*, Nat. Phys. **7**, 303 (2011).
[45] M. A. Griffith, A. S. T. Pires, and J. R. Sousa, Solid State Commun. **152**, 1850 (2012).
[46] F. B. Anderson and H. B. Callen, Phys. Rev. **136**, A1068 (1964).